Research Article

Nano Research
2024, 17(3): 1086–1093

ISSN 1998-0124 CN 11-5974/O4
https://doi.org/10.1007/s12274-023-5898-1

# Heteroatom doping regulates the catalytic performance of single-atom catalyst supported on graphene for ORR

Ji-Kai Sun[1], Yu-Wei Pan[1], Meng-Qian Xu[1], Lei Sun[1], Shaolong Zhang[2] (✉), Wei-Qiao Deng[1], and Dong Zhai[1] (✉)

[1] *Institute of Molecular Sciences and Engineering, Institute of Frontier and Interdisciplinary Science, Shandong University, Qingdao 266237, China*
[2] *College of Chemistry and Environmental Engineering, Shenzhen University, Shenzhen 518060, China*



**Received:** 29 March 2023 / **Revised:** 22 May 2023 / **Accepted:** 5 June 2023

## ABSTRACT

Replacing fossil fuels with fuel cells is a feasible way to reduce global energy shortages and environmental pollution. However, the oxygen reduction reaction (ORR) at the cathode has sluggish kinetics, which limits the development of fuel cells. It is significant to develop catalysts with high catalytic activity of ORR. The single-atom catalysts (SACs) of Pt supported on heteroatom-doped graphene are potential candidates for ORR. Here we studied the SACs of Pt with different heteroatoms doping and screened out Pt-$C_4$ and Pt-$C_3O_1$ structures with only 0.13 V overpotential for ORR. Meanwhile, it is found that B atoms doping could weaken the adsorption capacity of Pt, while N or O atoms doping could enhance it. This regularity was verified on Fe SACs. Through the electronic interaction analysis between Pt and adsorbate, we explained the mechanism of this regularity and further proposed a new descriptor named corrected d-band center ($\varepsilon_{d\text{-}corr}$) to describe it. This descriptor is an appropriate reflection of the number of free electrons of the SACs, which could evaluate its adsorption capacity. Our work provides a purposeful regulatory strategy for the design of ORR catalysts.

## KEYWORDS

single-atom catalyst (SAC), oxygen reduction reaction (ORR), heteroatom doping, corrected d-band center descriptor

## 1 Introduction

Due to the global energy shortage and environmental pollution, searching for alternatives to fossil fuels has become an urgent task. As a clean and efficient energy conversion device, fuel cells have attracted wide attention [1]. However, the electrochemical performance and energy conversion efficiency of fuel cells is hindered by the sluggish kinetics of oxygen reduction reaction (ORR) at the cathode [2, 3]. It is significant to design new cathode catalysts with high activity of ORR to improve the potential energy conversion efficiency. At present, Pt and Pt-based alloys are still the best cathode catalysts with high ORR activity [4–6]. Nonetheless, the high price and scarcity of Pt greatly increase the overall cost of fuel cells, thus limiting their widespread application in industry. Fortunately, the emergence of single-atom catalysts (SACs) provides a possibility for the large-scale application of Pt-based catalysts [7]. The SACs not only have high atomic utilization, reducing the amount of precious metal but also have the advantages of high selectivity, stable structure, and controllable configuration [8–10].

The properties of the SACs depend greatly on the support [11–13]. The metal–support interaction could induce the electron transfer between the metal and the support, regulate the electron state of the metal, and optimize the adsorption of intermediate species, which plays a crucial role in the catalytic reaction [14]. Carbon is considered to be one of the best supporting materials in electrocatalytic reactions, due to its high conductivity, low cost, and high electrochemical stability [15, 16]. Theoretically, the graphene structure is often used to represent a single layer of carbon material [17]. Typically, metal atoms could be anchored on the defects of graphene through tri-coordination, tetrcoordination, or pentatcoordination [18–20]. Tetrcoordination is the most common coordination mode, which is stable and highly active [21–26]. Therefore, the model used in this paper was the SACs that Pt fixed on graphene by tetrcoordination. In particular, the performance of SACs supported on graphene could be effectively regulated by heteroatomic doping [27]. N-doped graphene catalysts have been widely reported [28–30]. The catalytic activity of the catalyst could be improved by adjusting the number of N atoms [31, 32]. In addition, graphene catalysts doped by O and B atoms have also been reported [33–38]. However, previous studies have focused on the regulation of metals on a specific support [1, 16, 39, 40]. In this work, we focus on the effect of different doped atoms on the properties of certain metal SACs.

We designed a series of SACs of Pt supported on graphene with different heteroatom doping to explore the influence of heteroatomic doping on its ORR activity. Two models with excellent catalytic performance of ORR were found. Moreover, we found that the adsorption capacity could be regulated by different heteroatomic doping, and we further verified this regulation regularity on other metal SACs. Besides, the electronic interaction between the Pt and adsorbates was investigated to explain the adsorption mechanism. Finally, we proposed a new descriptor based on the d-band center and valence electron number of doped atoms, which is a good descriptor of adsorption capacity for SACs. Our calculation results provided theoretical guidance for the regulation of catalysts.

Address correspondence to Shaolong Zhang, shaolongzhang@outlook.com; Dong Zhai, zhaidong@sdu.edu.cn

清華大學出版社 Tsinghua University Press Springer

## 2 Computational methods

First-principles calculations based on density functional theory (DFT) were performed on the Vienna *an initio* simulation package (VASP) [41, 42]. The projector-augmented wave (PAW) potentials [43, 44] were adopted to treat the electron–ion interaction. And we applied the generalized gradient approximation (GGA) with the Perdew–Burke–Ernerhof (PBE) [45] realization to characterize the exchange and correlation potential [46]. The DFT-D3 method of Grimme [47] was employed to correct the intermolecular van der Waals (vdW) interaction. The energy cutoff was set as 500 eV to ensure precision. The convergence criteria for energy and force were respectively $10^{-5}$ eV and 0.02 eV/Å in structure optimization. For frequency calculation, a more strict convergence criterion for energy was used as $10^{-6}$ eV. To evaluate the stability of the catalysts, *ab initio* molecular dynamics (AIMD) simulations were performed in an NVT ensemble and lasted for 10 ps with a time step of 2 fs at 800 K. The temperature was controlled by the Nosé–Hoover method [48, 49].

A 4 × 4 × 1 graphene hexagonal supercell with Pt coordinated structure was constructed. The lattice parameters are $a = b =$ 9.84 Å, which is in accordance with available theoretical and experimental results. A vacuum space of 15 Å was built along the $z$-axis to avoid artificial interactions between the periodic images and the sheet. Considering the time-cost and precision, the Brillouin zone was sampled using 4 × 4 × 1 Monkhorst–Pack [50] mesh for geometry optimization and 21 × 21 × 1 mesh for electronic structures.

The formation energy ($\Delta E_{form}$) was computed by the following equation

$$\Delta E_{form} = E_{SACs} - (E_{defect} + E_{bulk}/n) \quad (1)$$

where $E_{SACs}$, $E_{defect}$, and $E_{bulk}$ are the total energies of the surface with the metal atom, the defective surface without the metal atom, and the bulk of metal, respectively. The $n$ is the number of atoms in the metal bulk.

The Gibbs free energy change ($\Delta G$) of each intermediate versus the initial state under various electrode potentials was calculated as the following equation

$$\Delta G = \Delta E + \Delta E_{ZPE} - T\Delta S + \Delta G_U + \Delta G_{pH} \quad (2)$$

where $\Delta E$ is the change in energy calculated by DFT simulation. The $\Delta E_{ZPE}$ is the change in zero-point energy. The zero-point energy ($E_{ZPE}$) for each system is calculated by

$$E_{ZPE} = \frac{\sum_{i=1}^{N_F} N_A h\nu_i}{2} \quad (3)$$

with the catalyst surface fixed, where $N_F$ is the degree of vibrational freedom; $N_A$ is Avogadro's number; $h$ is Plank's constant; and $\nu_i$ is the vibrational frequency. For a free linear molecule, free non-linear molecule, and surface adsorbed molecule, $N_F$ is respectively $3N - 5$, $3N - 6$, and $3N$, where $N$ is the number of atoms in the molecule. The $\Delta S$ is the changes in entropy and the $T$ is the temperature. Here $T$ was set to 298.15 K. The $\Delta G_U$ is the free energy change caused by the applied potential

$$\Delta G_U = -neU \quad (4)$$

where $n$ is the electron of such state and $U$ denotes the applied electrode potential versus the standard hydrogen electrode potential. $\Delta G_{pH}$ denotes the effect of pH value on free energy change.

$$\Delta G_{pH} = -2.303 k_B T \times pH \quad (5)$$

in which $k_B$ and $T$ respectively denote the Boltzmann constant and the temperature. All the simulations in this article are carried out at $T$ = 298.15 K and pH = 0.

## 3 Results and discussion

### 3.1 Model design

We constructed a series of SAC that Pt atoms supported on graphene. As shown in Fig. 1(a), the Pt atom was loaded on the graphene defect by four coordination bonds. To investigate the effect of heteroatom doping on the properties of the catalyst, different numbers of heteroatoms (B, N, and O) were doped to replace the C atoms coordinated with Pt, named Pt-$C_{4-x}Z_x$ (Z = B, N, and O, $x$ = 0, 1, 2, 3, and 4). When two heteroatoms were doped, there were three possible configurations. Two heteroatoms could replace the C atoms at 12, 13, and 14 sites, respectively. For clarification, the SAC of Pt where C atoms at position 12 sites replaced by Z atoms was named Pt-$C_2Z_2$-12. To evaluate the stability of various Pt-$C_{4-x}Z_x$ models, the formation energy ($\Delta E_{form}$) was calculated [51]. The lower the $\Delta E_{form}$, the more stable the structure. The $\Delta E_{form}$ of Pt(111) surface was also calculated as a reference. The relation between $\Delta E_{form}$ and the number of doped heteroatoms is shown in Fig. 1(b). Except for Pt-$C_1O_3$ and Pt-$O_4$, all Pt-$C_{4-x}Z_x$ models are stable. Thus, Pt-$C_1O_3$ and Pt-$O_4$ are not considered in the following ORR simulation.

In addition, the insightful correlation between $\Delta E_{form}$ and the number of doped heteroatoms was also investigated at the electronic level. It could be seen from the electron localization function (ELF) [52] plots in Fig. S1 in the Electronic

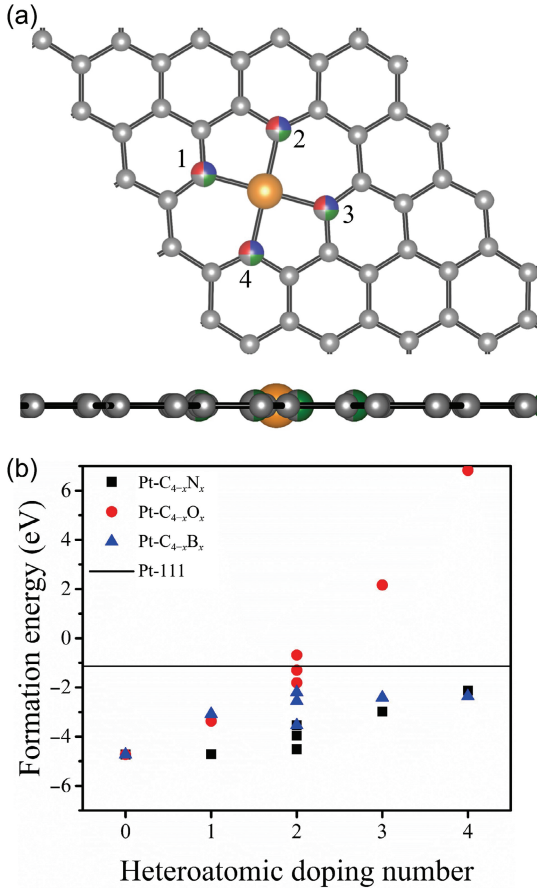


**Figure 1** Structure and formation energy (a) top and side views of the geometry structure of Pt-$C_{4-x}Z_x$ (Z = B, N, and O; $x$ = 0, 1, 2, 3, and 4). Color code: Pt in gold, boron in green, carbon in gray, oxygen in red, and nitrogen in blue. (b) Variations of the formation energies of Pt-$C_{4-x}Z_x$ with the number of doping heteroatoms.

Supplementary Material (ESM) that the electron density between Pt and coordinated O atoms in Pt-$O_4$ is significantly lower than that of other Pt-$Z_4$ models. Thus, the electronic interaction between Pt and doped O atoms is weak. Figure S2 in the ESM shows the crystal orbital Hamilton population (COHP) [53] between Pt and the coordinated atom of Pt-$Z_4$. The negative value of COHP (blue part) indicates bonding interactions between atoms, while the positive value (red part) indicates antibonding interaction [54]. Among the four Pt-$Z_4$ models, the positive area of COHP between Pt and O under the Fermi level is the largest. Thus, the Pt–O bond is unstable. Besides, the molecular orbital (MO) of the valence band maximum (VBM) of Pt-$O_4$ shows that Pt and O form antibonding orbitals. Therefore, the energy of Pt-$O_4$ is high and unstable.

The structures and electronic properties of the various Pt-$C_{4-x}Z_x$ models are listed in Table S1 in the ESM. It could be seen from Table S1 in the ESM that N atoms doping could increase the Bader charge of Pt. While, the B atoms doping could significantly reduce the Bader charge of Pt and even make it negatively charged. Compared to Pt-$C_4$, some O-doped structures increase the charge of Pt, while others decrease it. For Pt-$C_3O_1$, Pt-$C_2O_2$-12, and Pt-$C_2O_2$-14, the Bader charges of Pt are lower than Pt-$C_4$. In addition, the d-band centers ($\varepsilon_d$) of Pt-$C_3N_1$ and Pt-$C_2N_2$ are higher than those of Pt-$C_4$, while the $\varepsilon_d$ of Pt-$C_1N_3$ and Pt-$N_4$ are lower. And, all the $\varepsilon_d$ of Pt-$C_{4-x}B_x$ are higher than Pt-$C_4$. The $\varepsilon_d$ of Pt-$C_3O_1$ is close to Pt-$C_4$. Compared with Pt-$C_4$, the $\varepsilon_d$ of Pt-$C_2O_2$ is descending. Figure S3 in the ESM shows the density of states (DOS) [55] of various Pt-$C_{4-x}Z_x$ models. According to the d-band center theory, the increase of $\varepsilon_d$ of metal is adverse to bond with adsorbate while the decrease of $\varepsilon_d$ is in favor of adsorbate adsorption. Therefore, we predicted that Pt-$C_3N_1$ and Pt-$C_2N_2$ have stronger adsorbate adsorption capacity than Pt-$C_4$, while other Pt-$C_{4-x}Z_x$ models have weaker adsorbate adsorption capacity than Pt-$C_4$.

### 3.2 ORR simulation

It is reported that ORR has two main reaction pathways, the dissociative pathway and the associative pathway [56]. Both pathways were considered. The reaction equations for the two routes were set out in the ESM [57]. Figure S4 in the ESM shows the structure of Pt-$C_4$ and the most stable adsorption configuration of various ORR intermediates on it. To analyze the ORR activity on different Pt-$C_{4-x}Z_x$ catalysts, the Gibbs free energies ($G$) of the adsorbed intermediates were calculated [15, 58]. The relationship between adsorption free energies of intermediates and $\Delta G$ in ORR is described in ESM. The adsorption free energies of intermediates and limiting potentials ($U_L$) for ORR reaction on various Pt-$C_{4-x}Z_x$ catalysts were calculated and listed in Table S2 in the ESM. $U_L$ is the maximum work potential of ORR. Theoretically, the best $U_L$ of ORR is 1.23 V [56]. And the overpotential ($\eta$) over a catalyst is defined as

$$\eta = 1.23 - U_L \quad (6)$$

The smaller the $\eta$, the higher the catalytic activity of the catalyst.

Figure 2 shows the free energy profiles of Pt-$C_{4-x}Z_x$ with top ORR performance. For the dissociative pathway, as shown in Figs. 2(a) and 2(b), both Pt-$C_4$ and Pt-$C_3O_1$ show excellent ORR activity. The $\eta$ of these two catalysts both are 0.13 V, which is lower than most reported ORR catalysts. Therefore, Pt-$C_4$ and Pt-$C_3O_1$ are potentially high-performance ORR catalysts. Figures 2(c) and 2(d) show the free energy profiles for the associative route of ORR. Among all kinds of Pt-$C_{4-x}Z_x$ catalysts, Pt-$C_4$ shows the best ORR activity. It exhibits a $U_L$ of 0.93 V, with 0.3 V overpotential. The catalytic activity of Pt-$C_4$ in the two ORR pathways is higher than that of most reported catalysts [4, 6, 10]. As a reference, the ORR on Pt(111) surface was calculated. The η of Pt (111) in both ORR pathways is 0.46 V, consistent with the reported value [59, 60]. Compared with Pt(111) surface, the catalytic activity of Pt-$C_4$ and Pt-$C_3O_1$ for ORR is significantly improved. To further prove the stability of the catalyst, AIMD simulations on the best two models were screened. Pt-$C_4$ and Pt-$C_3O_1$, as well as the model with the highest adsorption energy, Pt-$C_2O_2$-13, were performed. As shown in Fig. S5 in the ESM, energy fluctuations of the three structures are relatively stable in AIMD simulation. After 10 ps, the configurations did not break.

### 3.3 Regularity discussion

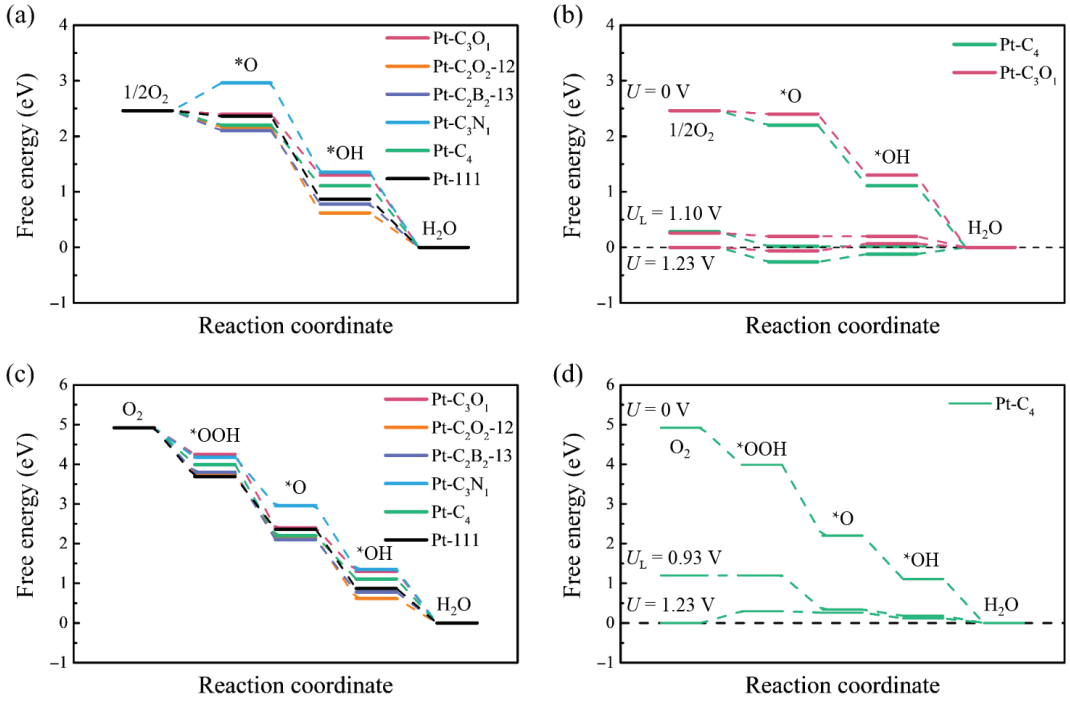


**Figure 2** The free energy profiles of ORR. (a) The dissociative pathway on different Pt-$C_{4-x}Z_x$, (b) the dissociative pathway on Pt-$C_4$ and Pt-$C_3O_1$ at different electrode potentials, (c) the associative pathway on different Pt-$C_{4-x}Z_x$ and (d) the dissociative pathway on Pt-$C_4$ at different electrode potential.

The $U_L$ of ORR depends on the adsorption energy of its intermediates. As shown in Fig. S6 in the ESM, the Gibbs free energies of OH ($G_{OH^*}$) and O ($G_{O^*}$) are roughly linearly correlated with $G_{OOH^*}$. But some data deviate from the line. Figure 3(a) is a contour plot for the $U_L$ in the dissociative path ($U_L$-dis) and the $G_{OH^*}$ and $G_{O^*}$ intermediates. Figure 3(b) shows the relationship between the $U_L$ in the associative path ($U_L$-ass) and the $G_{OOH^*}$ and $G_{OH^*}$. It could be concluded from Fig. 3 that either too high or too low adsorption free energy would decrease the $U_L$. When the Gibbs free energies of all ORR intermediates are 1.23 V, the $U_L$ could reach its theoretical limit. Therefore, adjusting the adsorption energy of intermediates is the key to improving the ORR catalytic activity of the catalyst.

However, the adsorption energy of intermediates in the ORR reaction is inconsistent with the predicted result according to the d-band center theory. Figure 4(a) shows the relationship between the Gibbs free energy of each intermediate and $\varepsilon_d$. In general, the adsorption free energy increases with the increase of the $\varepsilon_d$. The Pearson correlation coefficient between the adsorption Gibbs free energy of these three intermediates and $\varepsilon_d$ is close to 0.7. This indicates that the d-band center theory is not applicable to the metal atom of SACs, which has also been reported in other literature [61]. For metal clusters, the d-orbital electrons move freely throughout the cluster, so the metal center has enough vacant orbitals to receive the electrons of the adsorbed molecules. While for metal atoms in SACs, as shown in Fig. S1 in the ESM, electrons are localized around the metal. In this case, the adsorption capacity of the metal is limited by the number of vacant orbitals. The more electrons in d-orbitals, the fewer vacant orbitals, and the weaker the adsorption capacity. Thus, there is a positive correlation between the $\varepsilon_d$ and the d-orbital electron number of the metal atom, The higher the $\varepsilon_d$, the weaker the adsorption capacity.

Moreover, in metal bonds, d-orbital electrons are considered as free electrons, which can interact with the adsorbate. However, in SACs, as shown in Fig. S1 in the ESM, some electrons are localized in the Pt–Z bonds. We assume that those electrons do not interact with the adsorbed molecules. Therefore, for SACs, the d-orbital electrons of the metal could be divided into two parts: coordination electrons and free electrons. Coordination electrons are those coordinated with the support, not participating in the interaction with the adsorbate. The number of free electrons is equal to the total number of d-orbital electrons minus the number of coordination electrons. Only free electrons are involved in the bonding with the adsorbed molecules. As shown in Fig. S1 in the ESM, the electron localization density decreases in the order of Pt-$B_4$, Pt-$C_4$, Pt-$N_4$, and Pt-$O_4$. This indicates that different atomic dopants result in different numbers of coordination electrons. Compared to Pt-$C_4$, B doping increases the number of coordination electrons, while O and N doping reduces it. Besides, the heteroatoms coordinate with Pt in different ways. C atom and Pt each contribute one electron for coordination. And O or N atoms coordinate with Pt by providing lone pair electrons. While the electrons in the Pt–B coordination bond come mainly from Pt. Thus, we use the number of valence electrons of the dopant atoms to correlate with the number of the coordination electrons of Pt. Besides, $\varepsilon_d$ is a unanimously d-orbital electron descriptor. Based on $\varepsilon_d$, we have proposed a new descriptor called corrected d-band center ($\varepsilon_{d\text{-corr}}$), defined as

$$\varepsilon_{d\text{-corr}} = \varepsilon_d - 1.5(\nu_C - \nu_Z)n \quad (7)$$

where $\nu_Z$ and $\nu_C$ are respectively the valence electron number of the doped atom and C atom. $n$ is the number of doped atoms. The $\varepsilon_{d\text{-corr}}$ is a descriptor for the number of free electrons in metal for SACs.

In addition, the sites of heteroatom doping have a great effect on the structure and electronic properties. Figure S7 in the ESM illustrates the configurations of adsorbed O on Pt-$C_2Z_2$ and their charge density differences. The charge density differences of other intermediates on Pt-$C_3Z_1$ are listed in Fig. S8 in the ESM. There is a strong electron transfer between the ORR intermediates and the catalysts. Electrons are transferred from the catalysts to the intermediates. And, the amount of electron transfer varies with the heteroatom doping sites. Besides, the coordination environment of Pt may change after adsorbate adsorption, especially for Pt-$C_2O_2$, which has low formation energy. As shown in Fig. S7(c) in the ESM, the bond length of both Pt–O bonds in Pt-$C_2O_2$-12-O is 2.87 Å. And the bond lengths of Pt–O in Pt-$C_2O_2$-13-O are 2.20 and 2.63 Å, respectively. The coordination number of Pt-$C_2O_2$-12 and Pt-$C_2O_2$-13 are 2 and 3, respectively. The low coordination numbers of metal could reduce structural stability [23, 24]. Thus, the adsorption capacity of these two models is strong. In addition, for Pt-$C_3B_1$-OOH and Pt-$C_3B_1$-OH in Fig. S9 in the ESM, the O atom of adsorbate and doped B form an O–B bond, resulting in a decrease in energy. Regardless of these special cases, the Gibbs free energy of each adsorbate and the $\varepsilon_{d\text{-corr}}$ are fitted. As shown in Fig. 4(b), the adsorption free energy of each adsorbate and the $\varepsilon_{d\text{-corr}}$ are highly linearly correlated. The Pearson correlation coefficient between the $\varepsilon_{d\text{-corr}}$ and $G_{OOH^*}$, $G_{O^*}$, and $G_{OH^*}$ is 0.959, 0.934, and 0.927, respectively. Moreover, the regular residuals in Fig. S10 in the ESM show that the residuals of most data are within 0.5 eV. Particularly, residuals of $G_{OOH^*}$ are all within 0.3 eV.

Understanding the interaction between adsorbate and catalyst

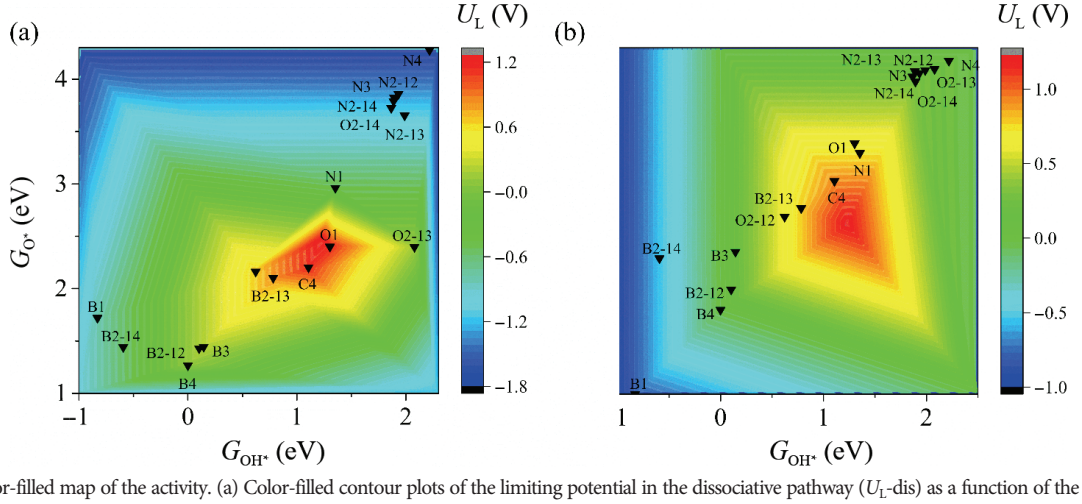


**Figure 3** Color-filled map of the activity. (a) Color-filled contour plots of the limiting potential in the dissociative pathway ($U_L$-dis) as a function of the $G_{O^*}$ and $G_{OH^*}$. (b) Color-filled contour plots of the limiting potential in the associative pathway ($U_L$-ass) as a function of the $G_{OOH^*}$ and $G_{OH^*}$. Pt-$C_{4-x}$ has been omitted for brevity.

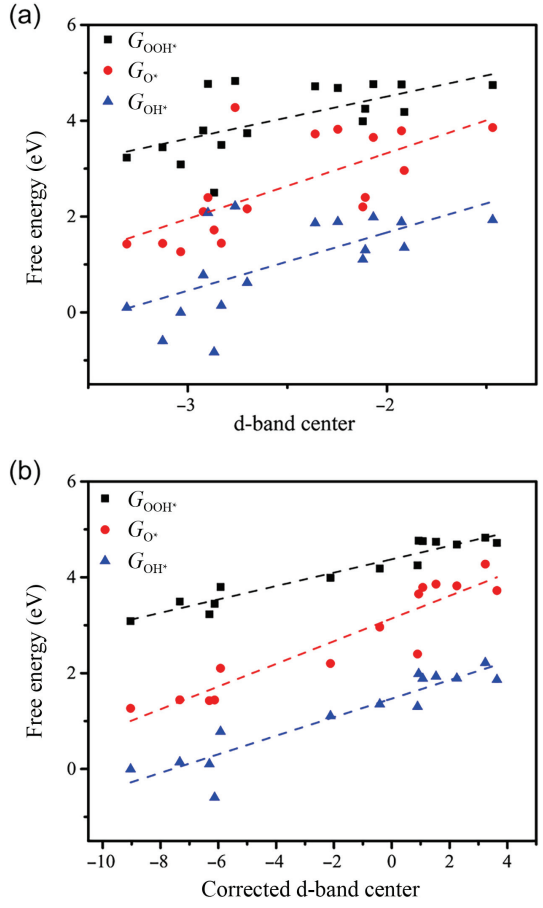


**Figure 4** The $G_{OOH^*}$, $G_{O^*}$, and $G_{OH^*}$ as a function of the (a) d-band center and (b) corrected d-band center.

active center at the microscopic level is the basis of regulating the interaction intensity. Figures S11 and S13 in the ESM show the MO diagrams of various Pt-$C_{4-x}Z_x$-O configurations. For most Pt-$C_{4-x}Z_x$-O, in the MO of the VBM and conduction band minimum (CBM), Pt and O interact as antibonds. Thus, the more free electrons in Pt, the more electrons fill the anti-bonding orbitals, resulting in weaker adsorption capability. We further calculated the COHP between Pt and adsorbed O to analyze their interaction. And the correlation between integrated COHP (ICOHP) and the $G_{O^*}$ was illustrated. COHP is obtained from DOS weighted by the elements of the Hamiltonian matrix. For non-bonding electrons, which do not participate in bonding, the Hamiltonian matrix is 0, resulting in a COHP of 0. Therefore, ICOHP could reflect the number of electrons involved in bonding, which corresponds to the free electrons. For the Pt–O bond, after the bonding orbitals are filled, the free electrons begin to occupy the anti-bonding orbitals. The more free electrons, the more electrons there are in the anti-bonding orbitals, leading to a larger ICOHP and adsorption energy. From the ICOHP in Fig. 5, it can be observed that the SACs with B doping exhibit a smaller ICOHP, while those with O and N doping display a larger ICOHP. Assuming that the number of electrons provided by the adsorbed O on Pt in different coordination environments is the same. This suggests that Pt coordinated with B has fewer free electrons, while Pt coordinated with O or N has more free electrons.

In summary, the $\varepsilon_{d\text{-}corr}$ that we came up with is a good descriptor for the number of free electrons of metal SACs. And, there is a high linear correlation between $\varepsilon_{d\text{-}corr}$ and adsorption energy of ORR intermediates. By calculating $\varepsilon_{d\text{-}corr}$, the adsorption strength of different catalysts could be easily predicted. Generally, B doping could reduce free electrons and enhance the adsorption capacity of the metal. While, O and N doping could increase free electrons and reduce the adsorption capacity. Therefore, in the experiment, the adsorption strength of metals on ORR intermediates could be controlled purposefully according to this strategy.

### 3.4 Rules verification

For Pt-$C_{4-x}Z_x$, we concluded that B doping could enhance its adsorption capacity, while O or N doping could weaken it. To verify the applicability of this rule to other metal SAC supported on carbon materials, another metal SAC was constructed for ORR simulation. Fe-$C_2N_2$-14 is one of the most widely reported ORR catalysts [62, 63]. Moreover, the electronic configurations of Fe and Pt are quite different. Therefore, we chose Fe for verification. The $\eta$ of ORR that we calculated on Fe-$C_2N_2$-14 is 0.99 V, which is close to the 1.05 and 1.00 V reported in Refs. [62, 63]. We find that the reason for the high $\eta$ on Fe-$C_2N_2$-14 is the strong adsorption energies of ORR intermediates. According to the rules that we have summarized, N and O atoms were doped to weaken its adsorption capacity. When the number of doped O was greater than 2, the catalyst was unstable, so it was not considered. As a reference, the ORR performance on Fe-$C_4$ was also simulated. The two kinds of ORR paths on the Fe-$C_{4-x}Z_x$ are shown in Fig. S14 in the ESM. It could be seen that the doping of N or O atoms effectively weakens the adsorption capacity of Fe-$C_4$ and improves its ORR catalytic activity. Among them, the $\eta$ of ORR on Fe-$N_4$ decreases to 0.68 V, exhibiting a good catalytic activity of ORR. It is exciting that the rule we proposed applies to Fe. This rule could be extended to most metal SACs supported on carbon materials. It provides a mechanism-specific strategy for the regulation of catalyst performance.

## 4 Conclusions

We designed a series of B, N, and O doped Pt SACs supported on graphene, named Pt-$C_{4-x}Z_x$. The catalytic activity of each Pt-$C_{4-x}Z_x$ for the two ORR pathways was calculated by the DFT method. Among them, we screened out Pt-$C_4$ and Pt-$C_3O_1$, which showed excellent catalytic performance in dissociative ORR pathways. The $\eta$ of the two catalysts are 0.13 V. It exhibits a better catalytic activity of ORR than most reported catalysts. Besides, the traditional d-band center theory may not apply to metal SACs. Given this, we proposed a new descriptor, $\varepsilon_{d\text{-}corr}$. The $\varepsilon_{d\text{-}corr}$ was a suitable descriptor of the number of free electrons for metal SACs. It has a good linear correlation with the adsorption performance of the catalyst. And, the internal relationship between the adsorption capacity and the electronic properties of the catalyst was investigated. The rationality of $\varepsilon_{d\text{-}corr}$ as a descriptor for free electron numbers was revealed. Moreover, we found that heteroatom has a regular effect on the $\varepsilon_{d\text{-}corr}$ of Pt-$C_{4-x}Z_x$. The B atoms doping could reduce the $\varepsilon_{d\text{-}corr}$ and enhance the adsorption capacity of Pt-$C_4$ to the ORR intermediates, while O or N doping could increase the $\varepsilon_{d\text{-}corr}$ and weaken its adsorption capacity. The generality of this rule has been verified with Fe-$C_{4-x}Z_x$. It provides a purposeful regulation strategy for improving the performance of metal SACs supported on carbon materials. Our work provided guidance for the adjustment of the adsorption properties of SACs.

## Acknowledgements

This work was supported by the National Key R&D Program of China (Nos. 2022YFA1503100 and 2022YFA1503102), the National Natural Science Foundation of China (No. 22273050), and the Natural Science Foundation of Shandong Province (Nos. YDZX2021001 and ZR2022MB098).

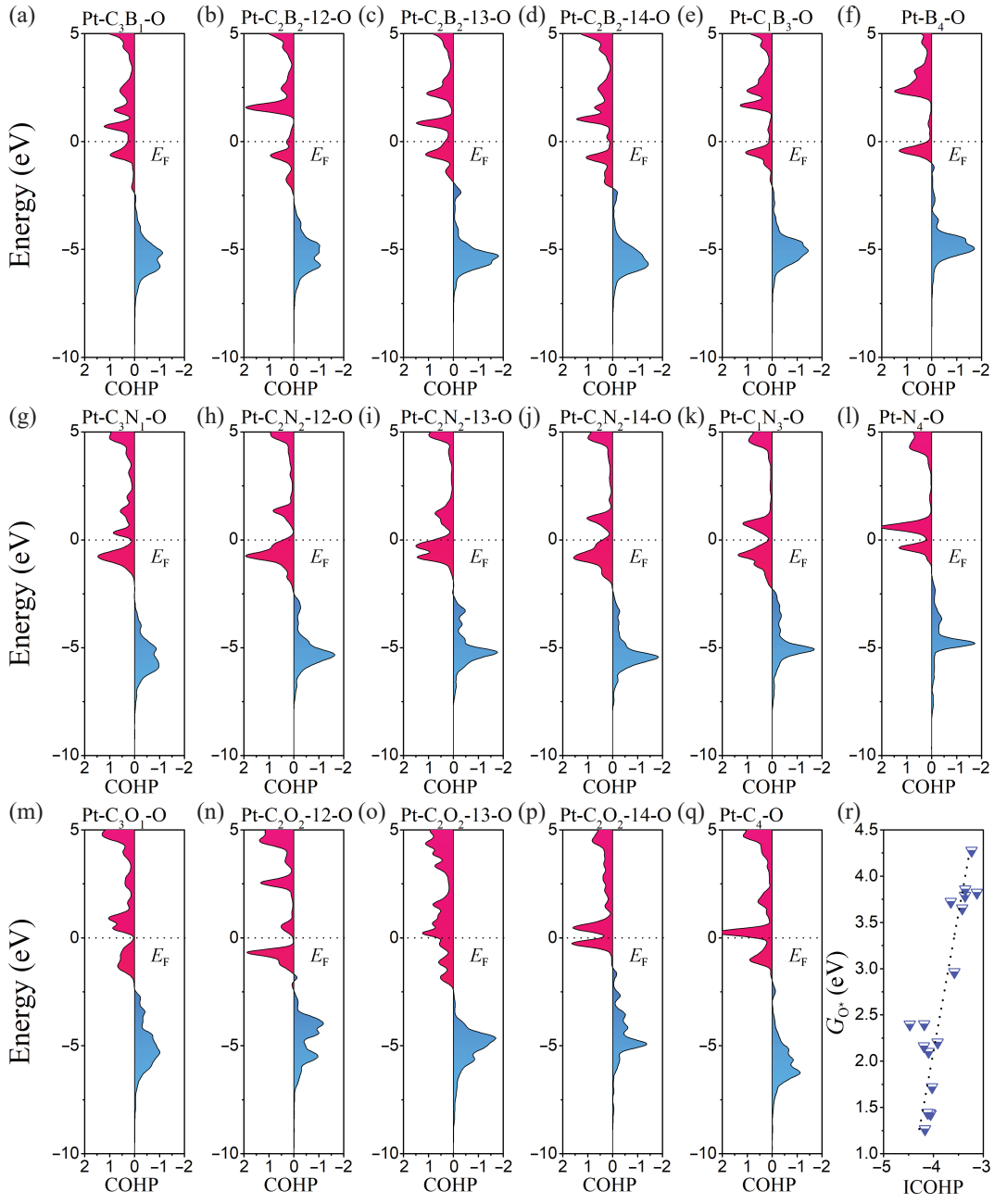


**Figure 5** (a)–(q) COHP between Pt and coordinated atoms of Pt-$C_{4-x}Z_x$-O. (r) The $G_{O^*}$ as a function of the ICOHP. The red part of the COHP denotes antibonding contributions, while the blue part denotes bonding contributions.

**Electronic Supplementary Material:** Supplementary material (tables, figures, and details for the two ORR pathways, calculation method and values of adsorption energy, properties of Pt-$C_{4-x}Z_x$, ELF, charge density differences, AIMD simulations, structures, and molecular orbitals) is available in the online version of this article at https://doi.org/10.1007/s12274-023-5898-1.

## References

[1] Liu, Q. T.; Li, Y. C.; Zheng, L. R.; Shang, J. X.; Liu, X. F.; Yu, R. H.; Shui, J. L. Sequential synthesis and active-site coordination principle of precious metal single-atom catalysts for oxygen reduction reaction and PEM fuel cells. *Adv. Energy Mater.* **2020**, *10*, 2000689.

[2] Wang, Y.; Wu, J.; Tang, S. H.; Yang, J. R.; Ye, C. L.; Chen, J.; Lei, Y. P.; Wang, D. S. Synergistic Fe-Se atom pairs as bifunctional oxygen electrocatalysts boost low-temperature rechargeable Zn-air battery. *Angew. Chem., Int. Ed.* **2023**, *62*, e202219191.

[3] Cui, T. T.; Wang, Y. P.; Ye, T.; Wu, J.; Chen, Z. Q.; Li, J.; Lei, Y. P.; Wang, D. S.; Li, Y. D. Engineering dual single-atom sites on 2D ultrathin N-doped carbon nanosheets attaining ultra-low-temperature zinc-air battery. *Angew. Chem., Int. Ed.* **2022**, *61*, e202115219.

[4] Lim, D. H.; Wilcox, J. Mechanisms of the oxygen reduction reaction on defective graphene-supported Pt nanoparticles from first-principles. *J. Phys. Chem. C* **2012**, *116*, 3653–3660.

[5] He, C. Y.; Zhang, J. J.; Shen, P. K. Nitrogen-self-doped graphene-based non-precious metal catalyst with superior performance to Pt/C catalyst toward oxygen reduction reaction. *J. Mater. Chem. A* **2014**, *2*, 3231–3236.

[6] Kan, D. X.; Lian, R. Q.; Wang, D. S.; Zhang, X. L.; Xu, J.; Gao, X. Y.; Yu, Y.; Chen, G.; Wei, Y. J. Screening effective single-atom ORR and OER electrocatalysts from Pt decorated MXenes by first-principles calculations. *J. Mater. Chem. A* **2020**, *8*, 17065–17077.

[7] Yang, X. F.; Wang, A. Q.; Qiao, B. T.; Li, J.; Liu, J. Y.; Zhang, T. Single-atom catalysts: A new frontier in heterogeneous catalysis. *Acc. Chem. Res.* **2013**, *46*, 1740–1748.

[8] Kim, J.; Kim, H. E.; Lee, H. Single-atom catalysts of precious metals for electrochemical reactions. *ChemSusChem* **2018**, *11*, 104–113.

[9] Chen, Y. J.; Ji, S. F.; Chen, C.; Peng, Q.; Wang, D. S.; Li, Y. D. Single-atom catalysts: Synthetic strategies and electrochemical

applications. *Joule* **2018**, *2*, 1242–1264.
[10] Ren, S.; Cao, X.; Jiang, Z. N.; Yu, Z. J.; Zhang, T. T.; Wei, S. H.; Fan, Q. K.; Yang, J.; Mao, J. J.; Wang, D. S. Single-atom catalysts for electrochemical applications. *Chem. Commun.* **2023**, *59*, 2560–2570.
[11] Yang, G. G.; Zhu, J. W.; Yuan, P. F.; Hu, Y. F.; Qu, G.; Lu, B. A.; Xue, X. Y.; Yin, H. B.; Cheng, W. Z.; Cheng, J. Q. et al. Regulating Fe-spin state by atomically dispersed Mn-N in Fe-N-C catalysts with high oxygen reduction activity. *Nat. Commun.* **2021**, *12*, 1734.
[12] Li, Y. Y.; Zhu, X. R.; Li, L.; Li, F. Y.; Zhang, X. Y.; Li, Y. F.; Zheng, Z. P. Study on the structure–activity relationship between single-atom, cluster and nanoparticle catalysts in a hierarchical structure for the oxygen reduction reaction. *Small* **2022**, *18*, 2105487.
[13] Zhu, P.; Xiong, X.; Wang, D. S. Regulations of active moiety in single atom catalysts for electrochemical hydrogen evolution reaction. *Nano Res.* **2022**, *15*, 5792–5815.
[14] Jing, H. Y.; Zhu, P.; Zheng, X. B.; Zhang, Z. D.; Wang, D. S.; Li, Y. D. Theory-oriented screening and discovery of advanced energy transformation materials in electrocatalysis. *Adv. Powder Mater.* **2022**, *1*, 100013.
[15] Jiao, Y.; Zheng, Y.; Jaroniec, M.; Qiao, S. Z. Origin of the electrocatalytic oxygen reduction activity of graphene-based catalysts: A roadmap to achieve the best performance. *J. Am. Chem. Soc.* **2014**, *136*, 4394–4403.
[16] Wang, Z. X.; Zhao, J. X.; Cai, Q. H. $CO_2$ electroreduction performance of a single transition metal atom supported on porphyrin-like graphene: A computational study. *Phys. Chem. Chem. Phys.* **2017**, *19*, 23113–23121.
[17] Wu, L. Y.; Wang, Q.; Yang, C. H.; Quhe, R.; Guan, P. F.; Lu, P. F. Crown oxygen-doping graphene with embedded main-group metal atoms. *Eur. Phys. J. B* **2018**, *91*, 46.
[18] Zhang, S. L.; Ao, X.; Huang, J.; Wei, B.; Zhai, Y. L.; Zhai, D.; Deng, W. Q.; Su, C. L.; Wang, D. S.; Li, Y. D. Isolated single-atom Ni-$N_5$ catalytic site in hollow porous carbon capsules for efficient lithium-sulfur batteries. *Nano Lett.* **2021**, *21*, 9691–9698.
[19] Sun, T. T.; Zhao, S.; Chen, W. X.; Zhai, D.; Dong, J. C.; Wang, Y.; Zhang, S. L.; Han, A. J.; Gu, L.; Yu, R. et al. Single-atomic cobalt sites embedded in hierarchically ordered porous nitrogen-doped carbon as a superior bifunctional electrocatalyst. *Proc. Natl. Acad. Sci. USA* **2018**, *115*, 12692–12697.
[20] Chen, J. W.; Zhang, Z. S.; Yan, H. M.; Xia, G. J.; Cao, H.; Wang, Y. G. Pseudo-adsorption and long-range redox coupling during oxygen reduction reaction on single atom electrocatalyst. *Nat. Commun.* **2022**, *13*, 1734.
[21] Chen, H.; Liang, X.; Liu, Y. P.; Ai, X.; Asefa, T.; Zou, X. X. Active site engineering in porous electrocatalysts. *Adv. Mater.* **2020**, *32*, 2002435.
[22] Garlyyev, B.; Fichtner, J.; Piqué, O.; Schneider, O.; Bandarenka, A. S.; Calle-Vallejo, F. Revealing the nature of active sites in electrocatalysis. *Chem. Sci.* **2019**, *10*, 8060–8075.
[23] Ortiz-Medina, J.; Wang, Z. P.; Cruz-Silva, R.; Morelos-Gomez, A.; Wang, F.; Yao, X. D.; Terrones, M.; Endo, M. Defect engineering and surface functionalization of nanocarbons for metal-free catalysis. *Adv. Mater.* **2019**, *31*, 1805717.
[24] Zhuo, H. Y.; Zhang, X.; Liang, J. X.; Yu, Q.; Xiao, H.; Li, J. Theoretical understandings of graphene-based metal single-atom catalysts: Stability and catalytic performance. *Chem. Rev.* **2020**, *120*, 12315–12341.
[25] Wu, X.; Zhang, H. B.; Zuo, S. W.; Dong, J. C.; Li, Y.; Zhang, J.; Han, Y. Engineering the coordination sphere of isolated active sites to explore the intrinsic activity in single-atom catalysts. *Nano-Micro Lett.* **2021**, *13*, 136.
[26] Zhuang, Z. C.; Xia, L. X.; Huang, J. Z.; Zhu, P.; Li, Y.; Ye, C. L.; Xia, M. G.; Yu, R. H.; Lang, Z. Q.; Zhu, J. X. et al. Continuous modulation of electrocatalytic oxygen reduction activities of single-atom catalysts through p-n junction rectification. *Angew. Chem., Int. Ed.* **2023**, *62*, e202212335.
[27] Tang, C.; Chen, L.; Li, H. J.; Li, L. Q.; Jiao, Y.; Zheng, Y.; Xu, H. L.; Davey, K.; Qiao, S. Z. Tailoring acidic oxygen reduction selectivity on single-atom catalysts via modification of first and second coordination spheres. *J. Am. Chem. Soc.* **2021**, *143*, 7819–7827.
[28] Ha, M. R.; Kim, D. Y.; Umer, M.; Gladkikh, V.; Myung, C. W.; Kim, K. S. Tuning metal single atoms embedded in $N_xC_y$ moieties toward high-performance electrocatalysis. *Energy Environ. Sci.* **2021**, *14*, 3455–3468.
[29] Li, L.; Huang, R.; Cao, X. R.; Wen, Y. H. Computational screening of efficient graphene-supported transition metal single atom catalysts toward the oxygen reduction reaction. *J. Mater. Chem. A* **2020**, *8*, 19319–19327.
[30] Ding, Y. N.; Zhou, W.; Gao, J. H.; Sun, F.; Zhao, G. B. $H_2O_2$ Electrogeneration from $O_2$ electroreduction by N-doped carbon materials: A mini-review on preparation methods, selectivity of N sites, and prospects. *Adv. Mater. Interfaces* **2021**, *8*, 2002091.
[31] Zhou, Y. N.; Gao, G. P.; Kang, J.; Chu, W.; Wang, L. W. Transition metal-embedded two-dimensional $C_3N$ as a highly active electrocatalyst for oxygen evolution and reduction reactions. *J. Mater. Chem. A* **2019**, *7*, 12050–12059.
[32] Li, R. Z.; Wang, D. S. Understanding the structure–performance relationship of active sites at atomic scale. *Nano Res.* **2022**, *15*, 6888–6923.
[33] Sun, J. P.; Liang, X. D. Density functional study of oxygen reduction reaction on oxygen doped graphene. In *Proceedings of the International Conference on Logistics*, *Engineering*, *Management and Computer Science*, Shenyang, China, 2015, pp 586–591.
[34] Majidi, R.; Saadat, M.; Davoudi, S. Electronic properties of O-doped porous graphene and biphenylene carbon: A density functional theory study. *Rom. Rep. Phys.* **2017**, *69*, 509.
[35] Wang, Y. L.; Shi, R.; Shang, L.; Waterhouse, G. I. N.; Zhao, J. Q.; Zhang, Q. H.; Gu, L.; Zhang, T. R. High-efficiency oxygen reduction to hydrogen peroxide catalyzed by nickel single-atom catalysts with tetradentate $N_2O_2$ coordination in a three-phase flow cell. *Angew. Chem., Int. Ed.* **2020**, *59*, 13057–13062.
[36] Yang, Y.; Mao, K. T.; Gao, S. Q.; Huang, H.; Xia, G. L.; Lin, Z. Y.; Jiang, P.; Wang, C. L.; Wang, H.; Chen, Q. W. O-, N-atoms-coordinated Mn cofactors within a graphene framework as bioinspired oxygen reduction reaction electrocatalysts. *Adv. Mater.* **2018**, *30*, 1801732.
[37] Deng, C. F.; He, R. X.; Shen, W.; Li, M. Theoretical analysis of oxygen reduction reaction activity on single metal (Ni, Pd, Pt, Cu, Ag, Au) atom supported on defective two-dimensional boron nitride materials. *Phys. Chem. Chem. Phys.* **2019**, *21*, 18589–18594.
[38] Zhou, Y. N.; Gao, G. P.; Chu, W.; Wang, L. W. Transition-metal single atoms embedded into defective $BC_3$ as efficient electrocatalysts for oxygen evolution and reduction reactions. *Nanoscale* **2021**, *13*, 1331–1339.
[39] Zheng, X. B.; Li, B. B.; Wang, Q. S.; Wang, D. S.; Li, Y. D. Emerging low-nuclearity supported metal catalysts with atomic level precision for efficient heterogeneous catalysis. *Nano Res.* **2022**, *15*, 7806–7839.
[40] Li, W. H.; Yang, J. R.; Wang, D. S. Long-range interactions in diatomic catalysts boosting electrocatalysis. *Angew. Chem., Int. Ed.* **2022**, *61*, e202213318.
[41] Kresse, G.; Furthmüller, J. Efficiency of *ab-initio* total energy calculations for metals and semiconductors using a plane-wave basis set. *Comput. Mater. Sci.* **1996**, *6*, 15–50.
[42] Kresse, G.; Furthmüller, J. Efficient iterative schemes for *ab initio* total-energy calculations using a plane-wave basis set. *Phys. Rev. B* **1996**, *54*, 11169–11186.
[43] Blöchl, P. E. Projector augmented-wave method. *Phys. Rev. B* **1994**, *50*, 17953–17979.
[44] Kresse, G.; Joubert, D. From ultrasoft pseudopotentials to the projector augmented-wave method. *Phys. Rev. B* **1999**, *59*, 1758–1775.
[45] Perdew, J. P.; Burke, K.; Ernzerhof, M. Generalized gradient approximation made simple. *Phys. Rev. Lett.* **1996**, *77*, 3865–3868.
[46] Chen, X.; Ge, F.; Chen, T. T.; Lai, N. J. The effect of GGA functionals on the oxygen reduction reaction catalyzed by Pt(111) and $FeN_4$ doped graphene. *J. Mol. Model.* **2019**, *25*, 180.
[47] Grimme, S.; Ehrlich, S.; Goerigk, L. Effect of the damping function in dispersion corrected density functional theory. *J. Comput. Chem.*

**2011**, *32*, 1456–1465.
[48] Bussi, G.; Donadio, D.; Parrinello, M. Canonical sampling through velocity rescaling. *J. Chem. Phys.* **2007**, *126*, 014101.
[49] Nosé, S. A unified formulation of the constant temperature molecular dynamics methods. *J. Chem. Phys.* **1984**, *81*, 511–519.
[50] Monkhorst, H. J.; Pack, J. D. Special points for Brillouin-zone integrations. *Phys. Rev. B* **1976**, *13*, 5188–5192.
[51] Yan, M.; Dai, Z. X.; Chen, S. N.; Dong, L. J.; Zhang, X. L.; Xu, Y. J.; Sun, C. H. Single-iron supported on defective graphene as efficient catalysts for oxygen reduction reaction. *J. Phys. Chem. C* **2020**, *124*, 13283–13290.
[52] Lu, T.; Chen, F. W. Meaning and functional form of the electron localization function. *Acta Phys. Chim. Sin.* **2011**, *27*, 2786–2792.
[53] Deringer, V. L.; Tchougréeff, A. L.; Dronskowski, R. Crystal orbital Hamilton population (COHP) analysis as projected from plane-wave basis sets. *J. Phys. Chem. A* **2011**, *115*, 5461–5466.
[54] Liu, X.; Jiao, Y.; Zheng, Y.; Jaroniec, M.; Qiao, S. Z. Building up a picture of the electrocatalytic nitrogen reduction activity of transition metal single-atom catalysts. *J. Am. Chem. Soc.* **2019**, *141*, 9664–9672.
[55] Wang, V.; Xu, N.; Liu, J. C.; Tang, G.; Geng, W. T. VASPKIT: A user-friendly interface facilitating high-throughput computing and analysis using VASP code. *Comput. Phys. Commun.* **2021**, *267*, 108033.
[56] Kulkarni, A.; Siahrostami, S.; Patel, A.; Nørskov, J. K. Understanding catalytic activity trends in the oxygen reduction reaction. *Chem. Rev.* **2018**, *118*, 2302–2312.
[57] Ge, F.; Qiao, Q. G.; Chen, X.; Wu, Y. Probing the catalytic activity of M-$N_{4-x}O_x$ embedded graphene for the oxygen reduction reaction by density functional theory. *Front. Chem. Sci. Eng.* **2021**, *15*, 1206–1216.
[58] Wang, G. Z.; Li, Z. F.; Wu, W. K.; Guo, H.; Chen, C.; Yuan, H. K.; Yang, S. A. A two-dimensional h-BN/$C_2N$ heterostructure as a promising metal-free photocatalyst for overall water-splitting. *Phys. Chem. Chem. Phys.* **2020**, *22*, 24446–24454.
[59] Zhang, P.; Xiao, B. B.; Hou, X. L.; Zhu, Y. F.; Jiang, Q. Layered SiC sheets: A potential catalyst for oxygen reduction reaction. *Sci. Rep.* **2014**, *4*, 3821.
[60] Tripković, V.; Skúlason, E.; Siahrostami, S.; Nørskov, J. K.; Rossmeisl, J. The oxygen reduction reaction mechanism on Pt(111) from density functional theory calculations. *Electrochim. Acta* **2010**, *55*, 7975–7981.
[61] Fu, Z. M.; Yang, B. W.; Wu, R. Q. Understanding the activity of single-atom catalysis from frontier orbitals. *Phys. Rev. Lett.* **2020**, *125*, 156001.
[62] Yang, Y. W.; Li, K.; Meng, Y. N.; Wang, Y.; Wu, Z. J. A density functional study on the oxygen reduction reaction mechanism on $FeN_2$-doped graphene. *New J. Chem.* **2018**, *42*, 6873–6879.
[63] Zhao, T. T.; Tian, Y.; Wang, Y. L.; Yan, L. K.; Su, Z. M. Mechanistic insight into electroreduction of carbon dioxide on $FeN_x$ ($x$ = 0–4) embedded graphene. *Phys. Chem. Chem. Phys.* **2019**, *21*, 23638–23644.